Carbon-Coated Core–Shell Fe–Cu Nanoparticles as Highly Active and Durable Electrocatalysts for a Zn–Air Battery

Gyutae Nam,[†] Joohyuk Park,[†] Min Choi,[‡] Pilgun Oh,[†] Suhyeon Park,[†] Min Gyu Kim,[§] Noejung Park,[‡] Jaephil Cho,[*,†] and Jang-Soo Lee[*,†]

[†]School of Energy and Chemical Engineering and [‡]Department of Physics, School of Natural Science Center for Multidimensional Carbon Materials, Ulsan National Institute of Science and Technology (UNIST), 689-798 Ulsan, South Korea and [§]Beamline Research Division, Pohang Accelerator Laboratory, Pohang University of Science and Technology, 790-784 Pohang, South Korea

ABSTRACT Understanding the interaction between a catalyst and oxygen has been a key step in designing better electrocatalysts for the oxygen reduction reaction (ORR) as well as applying them in metal–air batteries and fuel cells. Alloying has been studied to finely tune the catalysts' electronic structures to afford proper binding affinities for oxygen. Herein, we synthesized a noble-metal-free and nanosized transition metal CuFe alloy encapsulated with a graphitic carbon shell as a highly efficient and durable electrocatalyst for the ORR in alkaline solution. Theoretical models and experimental results demonstrated that the CuFe alloy has a more moderate binding strength for oxygen molecules as well as the final product, OH^-, thus facilitating the oxygen reduction process. Furthermore, the nitrogen-doped graphitic carbon-coated layer, formed catalytically under the influence of iron, affords enhanced charge transfer during the oxygen reduction process and superior durability. These benefits were successfully confirmed by realizing the catalyst application in a mechanically rechargeable Zn–air battery.

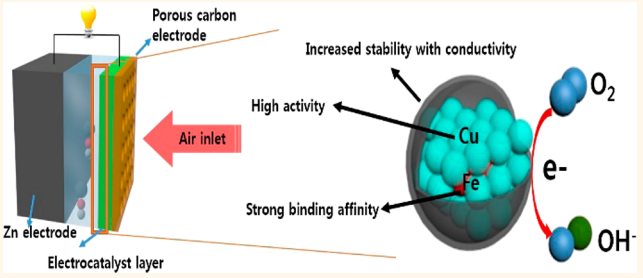

KEYWORDS: oxygen reduction reaction · Zn–air battery · transition metal alloy · durable electrocatalyst · binding affinity

Oxygen reactions are vital for metal–air batteries and fuel cells.[1,2] The fact that oxygen does not need to be stored within these size-limited devices enables them to have energy densities larger than those of Li-ion batteries. The sluggish rate for the oxygen reduction reaction (ORR) causes significant polarization loss, so proper catalysis of this reaction has been a critical issue. Although the ORR transformation comprises multiple electron transfer and chemical steps, the adsorption of O_2 is one of the major processes. Thus, it is reasonable to consider the interactions between oxygen molecules and the catalyst surface to achieve more moderate binding energies.

To optimize oxygen electrochemistry, the electronic structures of noble-metal-based catalysts have been extensively fine-tuned both experimentally and theoretically.[3–8] For example, a well-defined alloy of Pt with other transition metal nanoparticles (NPs) has much better catalytic activity and durability than Pt metal alone, even with much more enhanced mass activity.[9–12] However, it is still quite challenging to develop noble-metal-free alloy catalysts with comparable catalytic activity and durability.[13,14]

To prepare better non-precious-metal catalysts, volcano plots can provide useful guidelines for the design of reasonable catalysts that address the foregoing issues.[15] For example, theoretical calculations imply that Cu has the highest activity for oxygen reduction among the transition metals, whereas Fe has a strong binding affinity with oxygen. In previous studies, bi-core CuFe–N_x/C[16,17] demonstrated catalytic activity in the ORR, albeit with poor durability, which was attributed to the change in the oxidation number of metal–*N* bonds that can lead to morphological defects. Therefore, this catalyst is not yet suitable

* Address correspondence to jpcho@unist.ac.kr, linastar24@gmail.com.

Received for review April 15, 2015 and accepted May 12, 2015.

Published online May 13, 2015
10.1021/acsnano.5b02266

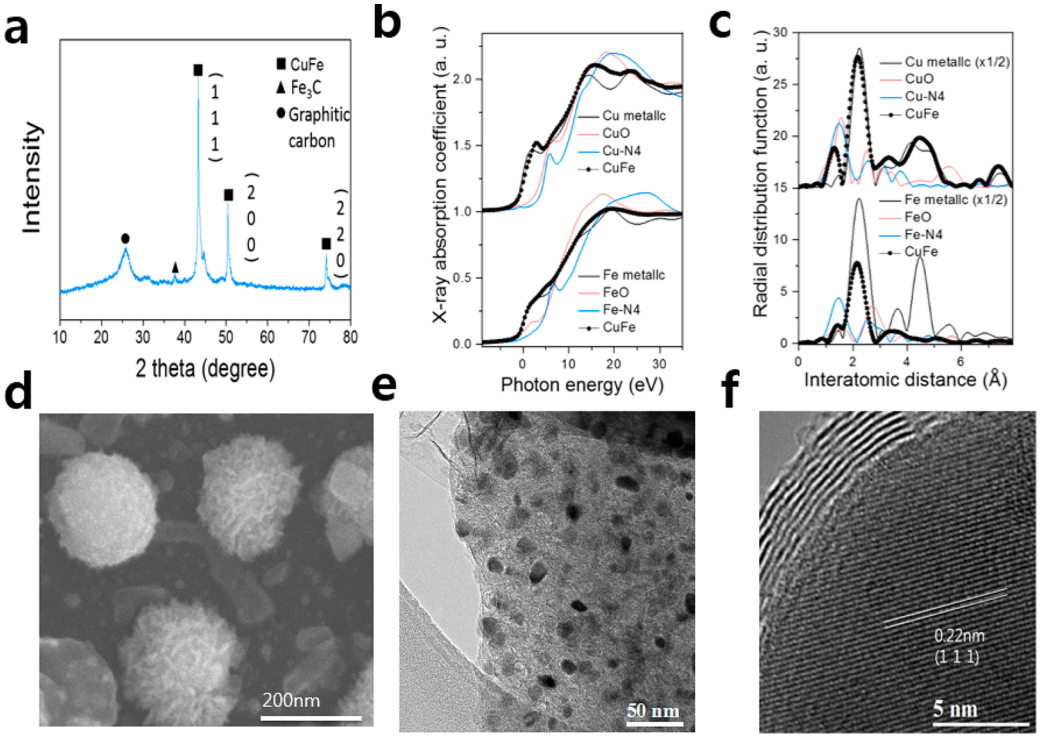

Figure 1. Material characterization of the CuFe alloy. (a) XRD data of CuFe, (b,c) extended X-ray absorption fine structure and X-ray absorption near edge structure analysis, (d) scanning electron microscopy image of CuFe, (e) low-magnification HR-TEM image of CuFe, and (f) high-magnification HR-TEM image of CuFe.

for practical application. Nitrogen-coordinated iron-based complexes have been studied as promising non-precious-metal catalysts for decades,[18−20] but the nature of their active sites is still unclear, although coordinated Fe can be considered as the active site.[21,22] In this work, we successfully synthesized CuFe alloy NPs coated with graphitic carbon shells *via* high-temperature pyrolysis using a copper phthalocyanine-based precursor and an iron acetylacetonate. The structural and electronic properties of this material were characterized both experimentally and theoretically in the context of its active sites, kinetic behavior, and overall electrochemical performance toward the ORR in an alkaline electrolyte. These graphitic-shell-coated CuFe NPs exhibit comparable activity and better stability for the ORR *versus* the Pt catalysts for both half-cell and Zn−air batteries. We believe that the Fe atoms embedded in the Cu-rich alloy afford moderate binding affinity for oxygen molecules and OH^- ions, while electron transfer through the graphitic carbon shell is simultaneously enhanced.

RESULTS

The X-ray diffraction (XRD) pattern of the CuFe catalyst prepared at 800 °C (hereafter designated CuFe, Figure 1a) matches that of the metallic CuFe alloy well.[23] The observed peaks at 2θ = 43.32, 50.46, and 74.14° (JCPDS no. 03-065-7002) correspond to reflections from the 111, 200, and 220 planes, respectively, and are slightly shifted from heat-treated chlorophyllin with satellite peaks around these main peaks. This indicates that some copper atoms in the lattice have been substituted by iron, thus affecting the lattice parameters of the Cu (Supporting Information Figure S1).[24] The crystalline structure of the CuFe alloy is still cubic and composed of Cu atoms with partial Fe substitution. In addition, the CuFe alloy catalyst contains iron carbide (Fe_3C) species and partial graphitic carbon structures at 24° from the (002) diffraction in its XRD pattern, but the intensity of the Fe_3C peak is substantially lower than those for the major CuFe alloy component. This means that the exact composition of the alloy cannot be determined using inductively coupled plasma (ICP) or thermogravimetric analysis (TGA) techniques due to the Fe_3C impurity.

More detailed structural information for the CuFe alloy is revealed with the extended X-ray absorption fine structure (EXAFS) analysis (Figure 1b,c). The normalized Cu and Fe K-edge peaks and radial distribution functions (RDF) of the alloy are clearly similar to those of metallic Fe and Cu, indicating that the as-prepared alloy does not contain Cu−N and Fe−N species. In addition, the intensity of each Fourier-transformed (FT) peak for the alloy in the RDFs is much lower than that in Cu and Fe metals, indicating the formation of a nanosized metallic alloy. For example, the FT peak intensity for Fe is lower than that of Cu and dramatically decreases at a higher *r* space, indicating the larger size of the Cu atoms compared to the Fe atoms in the alloy. This finding is also supported by the XRD data.

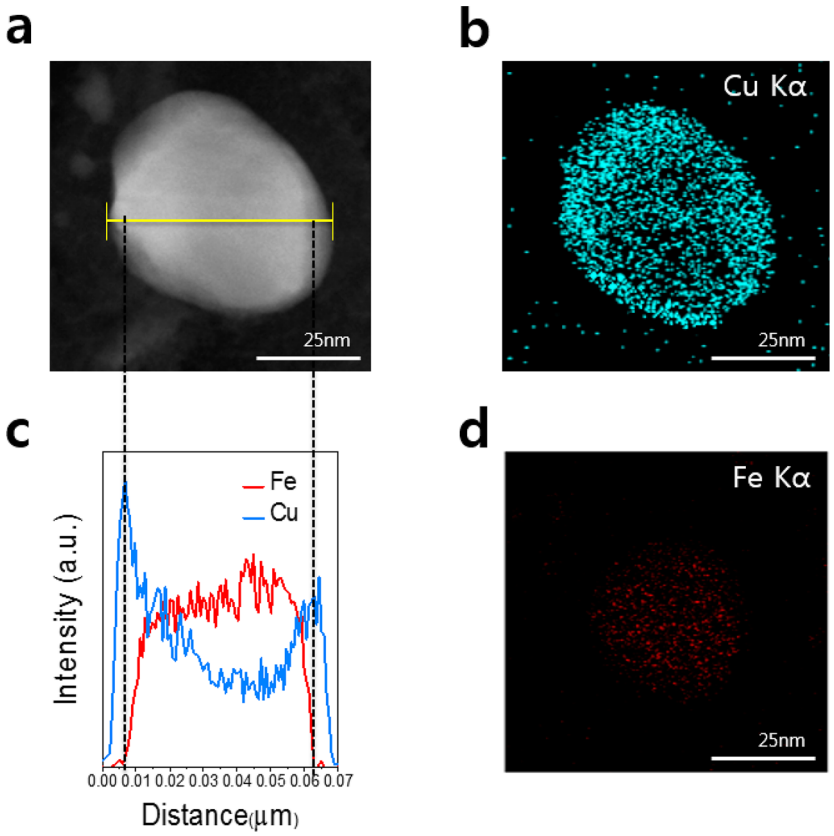

Figure 2. Structural and elemental analysis of the CuFe alloy. (a) High-angle annular dark field/STEM image of CuFe alloy nanoparticles and EDS elemental mapping of (b) Cu and (d) Fe in the same area. (c) EDS intensity profiles of yellow line in (a).

Furthermore, in contrast to the reference materials, this alloy has very different peaks derived from nitrogen-coordinated Cu and Fe complex such as Fe or Cu−N_4. Thus, nitrogen-coordinated Fe sites are not formed in this alloy; Fe cannot be affected by CN^- ions, and no degradation in activity is observed (unlike, in general, for Fe−N_4 structures) (Supporting Information Figure S2).[21] The detailed structural information from the EXAFS study also clearly supports the completely different structure of the as-prepared alloy compared to planar Fe-based catalysts and, therefore, the successful formation of the nanosized Cu−Fe alloy.

The high-resolution X-ray photoelectron spectroscopy (XPS) spectra of the N 1s, Fe 2p, and Cu 2p core levels for the CuFe alloy catalyst are shown in Supporting Information Figure S3. The presence of a N 1s peak at 398.8 eV indicates that copper phthalocyanine is fully decomposed by high-temperature annealing, forming N-doped carbon materials. Also, based on the absence of typical peaks due to metal nitride compounds at 398.0 eV, no copper−nitrogen bonding (Cu−N) is observed.[17] Although the intensities of the Fe-related XPS peaks are too weak to assign exactly, the Fe 2p peak at 720.0 eV could attributed to pure metallic Fe atoms.[25] However, the XPS peak shape clearly reveals that the oxidation state is not Fe(III), although its intensity is lower relative to that of Cu. This may be because most Fe atoms are under Cu atoms; our calculations showed that exposed Fe atoms in a CuFe alloy model are 1.225 eV higher in ground-state energy than the alloy model with buried Fe atoms, based on a supercell of $Cu_{44}Fe_4$ (Supporting Information). This structural information also suggests that Fe is not directly exposed to the external environment; that is, Fe is in an inner layer of the alloy rather than at the surface of Cu(111). This structural feature is also further supported by the scanning transmission electron microscopy (STEM) image and energy-dispersive X-ray spectroscopy (EDS) mapping (Figure 2). The XPS shows that most of the Cu atoms exist as pure metallic species with a small amount of CuO as an impurity (Supporting Information Figure S3). Cyclic voltammograms (CVs) of the CuFe alloy electrodes in Ar-saturated 0.1 M KOH reveal featureless redox peaks related to nitrogen-coordinated central Cu and Fe ions, except for a large capacitance current coming from the underlying carbon (Supporting Information Figure S4). These features provide evidence that the CuFe alloy structure has little structural information about the coordination of metal-surrounded N atoms.[17] Therefore, it can imply that the electronic state and local environment of the Cu atoms in the CuFe alloy are totally different from those in bi-core CuFe−N_x/C.[17] The conclusions from the high-resolution XPS correlated with the CV measurements suggest the presence of a metallic Cu and Fe alloy rather than N_xFe(III) and

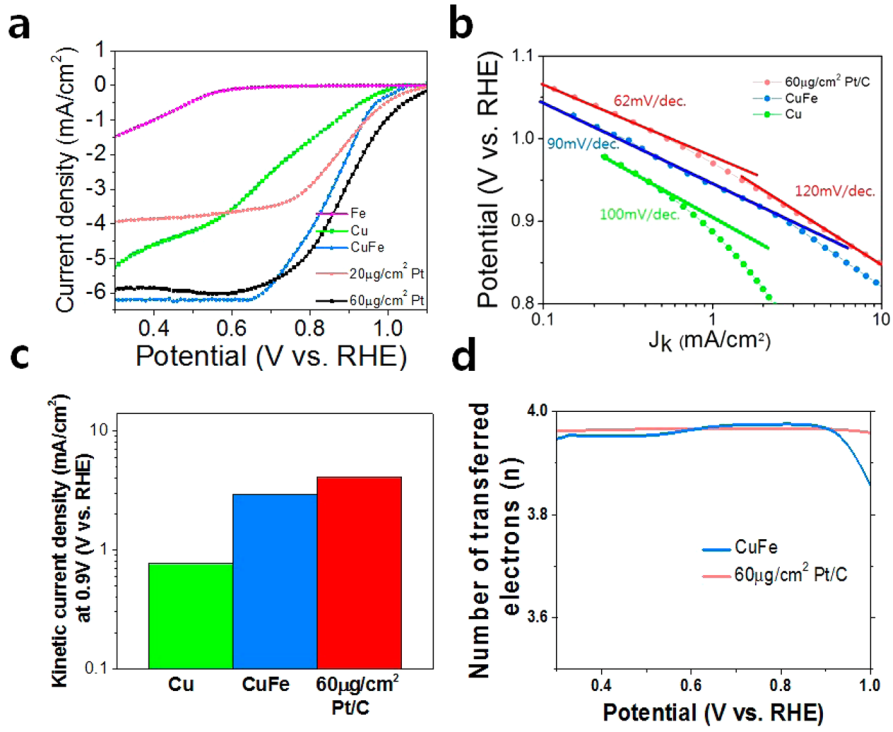

Figure 3. Electrocatalytic activity of the CuFe alloy. (a) Linear sweep voltammograms of CuFe, Cu, Fe, and Pt/C measured by a RRDE system. (b) Tafel plots of each catalyst. (c) Kinetic current at 0.9 V of each catalyst (except Fe in (b,c) due to low on-set potential of Fe). (d) Calculated number of transferred electrons of CuFe and Pt/C.

Cu(II)/Cu(I) compounds, so that it can be assumed that the ORR process for this alloy does not involve N_xFe(III) as the active site with Cu(II)/Cu(I) as the redox mediator.[16,17]

The morphology of the CuFe alloy was evaluated by scanning electron microscopy (SEM) and transmission electron microscopy (TEM). The as-prepared catalyst appeared as a nanosized metal alloy embedded in carbon ball-like microstructures (Figure 1d,e). Well-crystallized CuFe nanocrystals can be clearly observed at high magnification. The CuFe alloy exhibits a *d* spacing of 2.2 Å, corresponding to the (111) plane of the CuFe alloy. It was completely encapsulated inside a graphitic carbon shell, which serves as additional evidence of the metallic character of the metals (Figure 1f and Supporting Information Figure S5). To obtain more detailed information for this nanoparticle alloy, we prepared the cross section of a particle using a focused ion beam (FIB) technique and obtained the STEM image. The line mapping results indicate that Fe atoms are overlapped and mostly surrounded by Cu atoms, providing evidence of CuFe alloy formation, although Fe particles are more agglomerated than Cu in the inner area (Figure 2 and Supporting Information Figure S6). The high-resolution transmission electron microscopy (HR-TEM) image shows that the CuFe NPs are completely coated by a few layers of graphitic carbon sheets with a layer distance of 3.76 Å, and no free NPs are observed outside the carbon layers. The slightly increased (002) *d* spacing may be a notable clue for the incorporation of nitrogen into the graphitic layer, thus creating another active site (Supporting Information Figure S7).[26] The presence of well-developed graphene sheet coverings could impart enhanced electronic conductivity to this carbon-based CuFe alloy catalyst, although the thickness of the carbon walls may control the adsorption of O_2 and thus affect the ORR activity.[27] The degree of graphitization is also demonstrated by Raman spectroscopy. To better understand the onion-like graphitic carbon nanoshell layer, heat-treated Cu (chlorophyllin) has little graphitic carbon character and Cu_2O, which is totally different than the CuFe alloy (Supporting Information Figures S7 and S8). This means that Fe species can catalyze the graphitization of carbon.[26]

To verify the catalytic ORR activity of the CuFe electrocatalyst, we performed rotating ring-disk electrode (RRDE) measurements in O_2-saturated electrolyte solution (0.1 M KOH) at room temperature (Figure 3a). The copper precursor (chlorophyllin), heat-treated at 800 °C, shows much better ORR performance in 0.1 M KOH than the heat-treated Fe precursor (Fe(II) acetylacetonate). However, dramatically improved ORR activity for the CuFe alloy with the crystalline carbon sheets was achieved, which was comparable to that of Pt/C electrocatalysts, and well-defined limiting current density for the CuFe alloy is also observed, indicating that all of the catalysts are sufficiently active to reduce all of the oxygen molecules. The measured value of the Tafel slope for the CuFe catalyst was

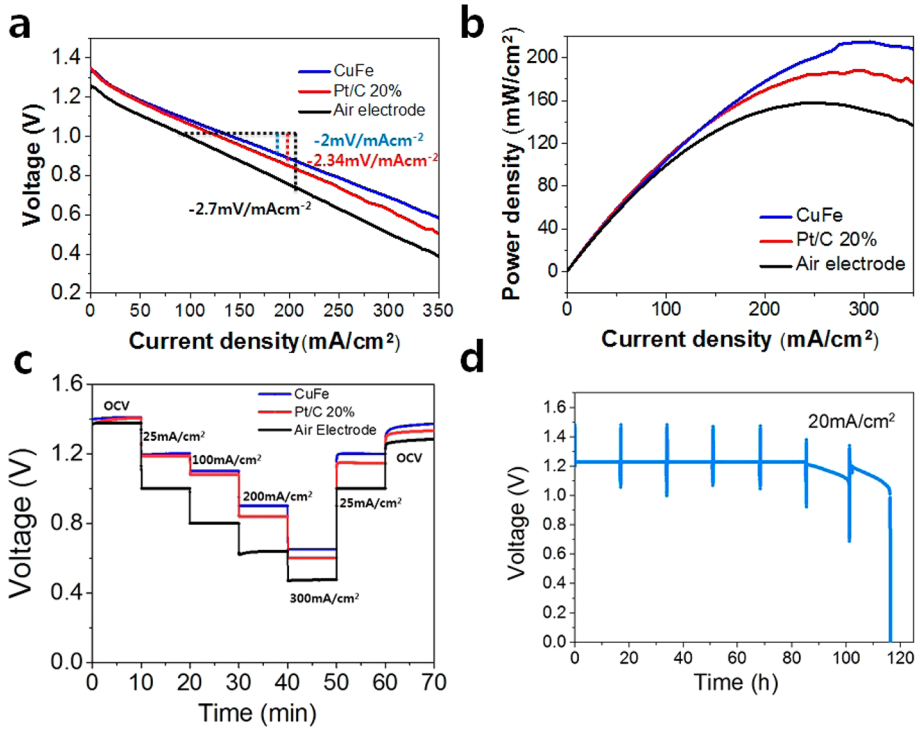

Figure 4. Zn−air battery application with a synthesized electrocatalyst. (a) Current−voltage (*I*−*V*) profile and (b) power density *versus* current density profile of Pt/C mixed-air electrode, CuFe mixed-air electrode, and air electrode without an electrocatalyst in the Zn−air battery. (c) Zn−air battery discharge profiles from low current density to high current density (includes OCV, 25, 100, 200, and 300 mA/cm^2). (d) Mechanically recharged Zn−air battery with CuFe electrocatalyst (20 mA/cm^2 of current density applied in ambient air conditions, with periodically recharged Zn plate and 6 M KOH).

90 mV dec^{-1}, which differs from dual slopes for Pt/C (~62 mV dec^{-1}). The difference in the Tafel slope values for these catalysts implies the different natures of their active sites. It can be concluded that the rate-determining steps during CuFe alloy catalysis of the ORR may be both the migration of intermediates and the electron transfer, based on its Tafel slope (Figure 3b).[26] We compared the kinetic currents for Fe, Cu, and CuFe catalysts at 0.9 V (*vs* RHE); CuFe showed a dramatically increased kinetic current, whereas those for Cu and Fe were much lower (Figure 3c). These results suggest that the affinity of hydroxyl groups, which control O_2 adsorption, for the CuFe alloy is lower than that for the single Cu- or Fe-based catalysts due to a reduced "blocking effect" of the active sites in the alloy.[28,29] This would result in a kinetic current density much higher than that for the single-component catalysts. The number of transferred electrons for the catalysts was calculated from the RRDE measurements (Supporting Information Figure S9); the calculated value for the CuFe alloy is ~3.7−3.9 (Figure 3d), which indicates that oxygen is reduced through a direct rather than an indirect pathway.

To reveal the durability of the CuFe electrocatalyst, we measured its chronoamperometric (*i*−*t*) response for the ORR (Supporting Information Figure S10a). As shown in its profile, CuFe shows much higher stability than Pt. This superior durability can further be supported by another durability test, cycling between 0.6 and 1.0 V at 50 mV s^{-1} under O_2-saturated conditions (Supporting Information Figure S10b), and its catalytic activity is maintained even after 10 000 continuous cycles. After the durability test, we investigated the morphological change of the CuFe electrocatalyst by HR-TEM. We could confirm that pristine CuFe morphology remained with the same crystal structure, although its graphitic carbon layers were completely turned into amorphous carbon (Supporting Information Figure S10c,d). Therefore, the carbon layer increases the corrosion resistance, affording excellent durability for the CuFe alloy. The enhanced stability for the alloy could be attributed to the corrosion resistance afforded by the carbon layers.

We also assembled a zinc−air battery with a CuFe alloy catalyst-functionalized porous electrode as the air cathode and Zn foil as the anode to demonstrate the potential of our catalyst for practical applications. A bare air electrode, a CuFe alloy, and the Pt/C catalyst embedded in the air cathode were prepared with the same electrode thickness and catalyst content and also tested under the same conditions for comparison. Figure 4a,b presents the polarization curves of each single cell and the peak power density of the Zn−air battery, with the CuFe alloy as the catalyst reaching 212 mW/cm^2, which is even higher than that of the Pt-catalyzed air electrode as well as the bare cathode. For more quantitative analysis, we compared each voltage drop rate and found that the slope of the CuFe

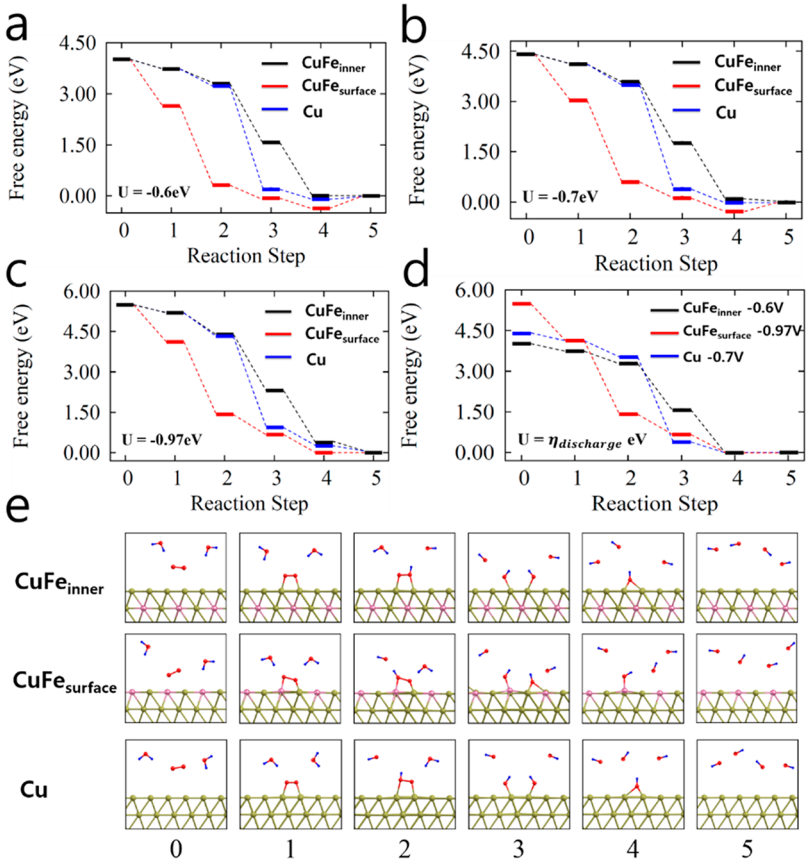

Figure 5. Free-energy diagram of intermediates during ORR for CuFe$_{inner}$, CuFe$_{surface}$, and Cu(111). All models (CuFe$_{inner}$, Cu, and CuFe$_{surface}$) turns downhill, which mean spontaneous reaction at (a) $U = -0.6$ eV, (b) $U = -0.7$ eV, and (c) $U = -0.97$ V, respectively. (d) Comparison of free energy for each model at an overpotential that can make the assumed reaction pathway spontaneous. (e) Assumed ORR reaction pathway for computational calculations.

alloy is -2 mV/mAcm^{-2}, which is lower than that of other electrodes (slope of Pt/C 20% is -2.34 mV/mAcm^{-2}), especially at a high current density above 100 mAcm^{-2} (Figure 4a and Supporting Information Figure S11). These benefits were also demonstrated by the excellent current step up and down response characteristics of the CuFe-alloy-catalyzed single Zn–air battery (Figure 4c). This means that the CuFe-alloy-catalyzed Zn–air cell can be applicable to automobile applications, which need fast dynamic response.[30]

After discharging, we found that the battery can be recharged by refueling the Zn anode and KOH electrolyte periodically. Therefore, the air electrode made with the CuFe alloy could work robustly for more than 100 h without any loss of voltage (Figure 4d), indicating again the high stability of the CuFe alloy catalyst. Polarization decrease after 100 h discharge may occur because generated heat during the discharge affects electro-osmosis of the electrolyte and the polytetrafluoroethylene (PTFE) hydrophobic binder, causing air electrode polarization loss due to more electrolyte infiltration into the air electrode. Furthermore, this decrease in hydrophobicity of PTFE can be accelerated in an alkaline KOH electrolyte, causing a decrease in three phase reaction sites.[31] This means that much more effort should be devoted to the development of whole air cathodes beyond preparation of electrocatalysts because the degradation mechanism of the air cathode mostly results from the air electrode itself under practical working conditions.

To confirm the active sites of the CuFe electrocatalyst, we treated the alloy with acid. The acid-leached sample no longer contained the CuFe alloy; however, small amounts of pyridinic-type nitrogen-doped carbon and Fe_3C were confirmed by XPS, XRD, and HR-TEM. Interestingly, these materials still have a little catalytic activity for ORR (Supporting Information Figures S12 and S13).[32,33] For example, the acid-treated nanoparticle alloy had an onset potential similar to that of the CuFe alloy; this may be attributed to the pyridinic nitrogen species, which are closely related to the onset potential.[34,35] The remaining Fe_3C species can also facilitate the ORR process,[32] but its contribution on catalytic activity is negligible due to its low contents. Therefore, it follows that the CuFe alloy contributes more significantly to ORR as a major active site than N-doped carbon shells and carbon-coated Fe_3C species. Based on the aforementioned discussion, it is reasonable to focus on how CuFe NPs interact with oxygen molecules, without considering the N-doped carbon and Fe_3C species.

To understand the positive attributes of the transition metal alloy, we performed density functional theory (DFT) calculations for the free energies of the intermediates during the ORR for the Cu and CuFe alloy systems, using the Vienna Ab Initio Simulation Package (VASP).[36−39] Such calculations can provide critical clues for elucidating the reaction pathway for the alloy-mediated ORR (Figure 5). The adsorption of O_2 is one of the major steps in the ORR, although the reaction involves complex processes associated with several oxygen-containing species in the alkaline media. Two models are popular for O_2 adsorption: end-on adsorption and the bridge model. End-on adsorption leads to a pathway through H_2O_2, and bridge adsorption results in a direct four-electron pathway. Based on our direct reduction pathway for the CuFe alloy catalyst, we adapted the bridge model, involving several intermediate species such as O_2, O_2*, OOH^-, and OH^-. We studied the interactions between O_2/OH^- and the catalyst surface with three alloy models: an Fe atom buried in the Cu alloy ($CuFe_{inner}$), an Fe atom exposed on the Cu alloy ($CuFe_{surface}$), and a reference Cu(111) substrate (Figure 5e). We compared the free energies of the intermediates at specific potentials which result in a downhill pathway for spontaneous reaction (Figure 5a−c). Among the three models, the $CuFe_{inner}$ model displays a downhill free-energy diagram with the lowest potential ($U = -0.6$ eV), compared to that of $CuFe_{surface}$ ($U = -0.97$ eV) and Cu ($U = -0.7$ eV), indicating that the ORR would be much more facilitated on the $CuFe_{inner}$ surface than on $CuFe_{surface}$ and Cu. Furthermore, from this theoretical study, these calculated reaction pathways indicate that the transformation from step 4 to step 5, OH^- ion desorption, could determine the overall kinetics for the ORR among all three models. The proper binding strength, not too strong or too weak, for the oxygen-related species can be successfully achieved by the Fe atoms embedded in the Cu metal alloy. This result also corresponds well with the measured Tafel slope of the alloy, as well as the enhanced kinetic current (Figure 3b,c). We believe that the alloy, with its inner Fe atoms, effectively decreases the binding energy for the OH^- ion during the ORR process, thus facilitating its kinetics compared to bare Cu and the alloy with surface Fe atoms (Supporting Information Figure S14). Therefore, it is reasonable to conclude that the as-prepared CuFe alloy catalyst is a bulk alloy-type material in which most of the Fe atoms are surrounded by Cu atoms (Figure 2). The electronic structure of the Fe can be properly tuned by the alloying with Cu, and thus, this characteristic feature could enable this bulk alloy to have CN tolerance and dramatically enhanced catalytic activity for the ORR by facilitating the desorption of OH^- from the alloy catalyst.

CONCLUSIONS

In conclusion, a noble-metal-free CuFe alloy encapsulated with graphitic carbon layers was synthesized by the pyrolysis of a copper phthalocyanine-based precursor and an iron acetylacetonate. The alloy was demonstrated to be a highly efficient and durable catalyst for the ORR. Physicochemical characterization confirmed the formation of a CuFe nanoalloy in which most of the Fe atoms were surrounded by Cu atoms, and Fe catalyzed the formation of a few well-developed graphene layers that fully covered the alloy. Electrochemical characterization indicated that the CuFe alloy had q catalytic activity much higher than that of pyrolyzed Cu and Fe. To demonstrate the synergistic effects due to alloying, we performed theoretical calculations for the CuFe alloy, an Fe-exposed alloy, and a metallic Cu model. Due to the moderated binding energies of oxygen-related species on the surface of the catalyst, the inner layer of the Fe-substituted $CuFe_{inner}$ alloy exhibited an overpotential lower than that of the other two models, in agreement with our experimental results. In addition, the N-doped graphitic carbon shells afford not only electrical conductivity but also durability during long-term oxygen reduction operation, rendering the CuFe alloy as a promising non-precious-metal electrocatalyst for alkaline-based mechanically rechargeable Zn−air batteries.

MATERIALS AND METHODS

Synthesis of CuFe Alloy Catalysts. Five grams of chlorophyllin (Sigma-Aldrich) and 2 g of iron acetylacetonate(II) were dissolved in a mixture solvent of distilled water and ethanol (1:1 v/v) and then dried at 100 °C. The fully dried catalyst precursor was fired at 800 °C (increasing 5 °C per 1 min) under Ar atmosphere for 1 h. The copper precursor (chlorophyllin) and the iron precursor (Fe(II) acetylacetonate) heat-treated at 800 °C under Ar atmosphere for 1 h are denoted as Cu and Fe, respectively.

Preparation of Catalyst Ink and Working Electrode. The formulation of catalyst ink is a mixture of 10 mg of the CuFe catalyst powder, 200 μL of 0.05% Nafion (Aldrich) solution, and 800 μL of ethanol. Briefly, desired catalyst ink was prepared by being ultrasonically mixed in distilled water for at least 1 h to form a homogeneous catalysts ink. Five microliters of ink was loaded on the surface of a polished glassy carbon working electrode, resulting in 0.389 mg_{cat}/cm^2. For the 60 $\mu g_{pt}/cm^2$ catalysts, 8 mg of 20% Pt/C powder was dissolved in 800 μL of water until fully dispersed, and 200 μL of 0.05% Nafion (Aldrich) solution was added for Pt/C catalyst ink. This desired catalyst ink was ultrasonically mixed for at least 1 h to obtain a homogeneous catalysts ink. Then, 5 μL of ink was loaded on the surface of the working electrode, resulting in 0.318 $mg_{(20\%\ Pt/C)}/cm^2$, corresponding to 60 $\mu g_{pt}/cm^2$ with the same methods mentioned above.

Electrochemical Measurements. Rotating ring-disk electrode (ALS Co., Ltd.) experiments were carried out using the desired catalyst film (deposited on a GC electrode) as the working electrode in 0.1 M KOH alkaline electrolyte with saturated O_2.

Pt wire and Hg/HgO were used as a counter and a reference electrode, respectively. Electrochemical characterization was conducted using a bipotentiostat (IviumStat). Before measuring the O_2 reduction current, we conducted cyclic voltammetry in the range of 0.15 to −0.6 V (*vs* Hg/HgO) with a 30 mV/s scan rate until a saturated current was obtained and measured its ORR current. The capacitive current was corrected by means of measuring a CV in Ar-saturated 0.1 M KOH. The collection efficiency (N) was determined under an Ar atmosphere using 10 mM $K_3[Fe(CN)_6]$, which is around 0.41. This value is very close to its theoretical value of 0.42. The number of electrons transferred (n) was calculated using the equations below.

$$n = 4\frac{I_d}{I_d + I_r/N}$$

All of the potential here is calibrated using the method described in our precious report[35] and converted to the RHE value by adding 0.929 V to the measured potential (*vs* Hg/HgO).

Kinetic Current Calculation. Kinetic currents of the electrocatalyst were obtained from mass transfer correction using the Levich equation.

$$i_{measured}^{-1} = i_k^{-1} + i_d^{-1}$$

shere $i_{measured}$ is the measured oxygen reduction current density, i_k is the kinetic current density, and i_d is the limiting current density.

Zn−Air Full-Cell Tests. For the full-cell test of our catalysts, we prepared a zinc plate as an anode, and 6 M KOH was used for the electrolyte. Cell guard 3501 membrane was used for a separator. The air cathode was prepared by a mixture of activated carbon (Darco G-60A, Sigma-Aldrich), PTFE binder (60 wt % PTFE emulsion in water, Sigma-Aldrich), and electrocatalyst in a ratio of 65:8:27, respectively. An assembled full-cell was performed at several discharge and charge currents.

Physical Characterization. The synthesized material morphology was examined using HR-TEM (JEOL JEM-2100F) operating at 200 kV. Powder analysis was performed using an X-ray diffractometer (D/Max2000, Rigaku). The oxidation state of the elements was analyzed using XPS (Thermo Scientific Kα spectrometer, 1486.6 eV), and the surface carbon state was examined using micro-Raman (WITec).

DFT Calculations. We investigated the electronic structure of Cu, $CuFe_{inner}$, and $CuFe_{surface}$ for calculation. We used VASP to calculate the ground state of many electron systems in the framework of density functional theory. The plane-wave basis set with an energy cut off of 400 eV and the PBE-type gradient-corrected exchange-correlation potential were employed. As a model system, we set a supercell which is made of the $4 \times 4 \times 3$ face-centered cubic Cu(111), and for two different types of alloy models, we set a supercell of $Cu_{44}Fe_4$.

Conflict of Interest: The authors declare no competing financial interest.

Acknowledgment. This work was supported by the next generation secondary battery R&D program of MKE/KEIT (10042575).

Supporting Information Available: Additional figures and experimental details as described in text. The Supporting Information is available free of charge on the ACS Publications website at DOI: 10.1021/acsnano.5b02266.

REFERENCES AND NOTES

1. Lee, J.-S.; Tai Kim, S.; Cao, R.; Choi, N.-S.; Liu, M.; Lee, K. T.; Cho, J. Metal−Air Batteries with High Energy Density: Li−Air *versus* Zn−Air. *Adv. Energy Mater.* **2011**, *1*, 34–50.
2. Cheng, F.; Chen, J. Metal−Air Batteries: From Oxygen Reduction Electrochemistry to Cathode Catalysts. *Chem. Soc. Rev.* **2012**, *41*, 2172–2192.
3. Stamenkovic, V.; Mun, B. S.; Mayrhofer, K. J. J.; Ross, P. N.; Markovic, N. M.; Rossmeisl, J.; Greeley, J.; Nørskov, J. K. Changing the Activity of Electrocatalysts for Oxygen Reduction by Tuning the Surface Electronic Structure. *Angew. Chem., Int. Ed.* **2006**, *118*, 2963–2967.
4. Greeley, J.; Stephens, I. E. L.; Bondarenko, A. S.; Johansson, T. P.; Hansen, H. A.; Jaramillo, T. F.; Rossmeisl, J.; Chorkendorff, I.; Nørskov, J. K. Alloys of Platinum and Early Transition Metals as Oxygen Reduction Electrocatalysts. *Nat. Chem.* **2009**, *1*, 552–556.
5. Gasteiger, H. A.; Kocha, S. S.; Sompalli, B.; Wagner, F. T. Activity Benchmarks and Requirements for Pt, Pt-Alloy, and Non-Pt Oxygen Reduction Catalysts for PEMFCs. *Appl. Catal., B* **2005**, *56*, 9–35.
6. Mukerjee, S.; Srinivasan, S.; Soriaga, M. P.; McBreen, J. Role of Structural and Electronic Properties of Pt and Pt Alloys on Electrocatalysis of Oxygen Reduction: An *In Situ* XANES and EXAFS Investigation. *J. Electrochem. Soc.* **1995**, *142*, 1409–1422.
7. Benson, J.; Xu, Q.; Wang, P.; Shen, Y.; Sun, L.; Wang, T.; Li, M.; Papakonstantinou, P. Tuning the Catalytic Activity of Graphene Nanosheets for Oxygen Reduction Reaction *via* Size and Thickness Reduction. *ACS Appl. Mater. Interfaces* **2014**, *6*, 19726–19736.
8. Yang, W.; Zhai, Y.; Yue, X.; Wang, Y.; Jia, J. From Filter Paper to Porous Carbon Composite Membrane Oxygen Reduction Catalyst. *Chem. Commun.* **2014**, *50*, 11151–11153.
9. Hernandez-Fernandez, P.; Masini, F.; McCarthy, D. N.; Strebel, C. E.; Friebel, D.; Deiana, D.; Malacrida, P.; Nierhoff, A.; Bodin, A.; Wise, A. M.; et al. Mass-Selected Nanoparticles of Pt_xY as Model Catalysts for Oxygen Electroreduction. *Nat. Chem.* **2014**, *6*, 732–738.
10. Stamenkovic, V. R.; Fowler, B.; Mun, B. S.; Wang, G.; Ross, P. N.; Lucas, C. A.; Markovic, N. M. Improved Oxygen Reduction Activity on $Pt_3Ni(111)$ *via* Increased Surface Site Availability. *Science* **2007**, *315*, 493–497.
11. Zhu, H.; Zhang, S.; Guo, S.; Su, D.; Sun, S. Synthetic Control of FePtM Nanorods (M = Cu, Ni) To Enhance the Oxygen Reduction Reaction. *J. Am. Chem. Soc.* **2013**, *135*, 7130–7133.
12. Kim, Y. S.; Jeon, S. H.; Bostwick, A.; Rotenberg, E.; Ross, P. N.; Stamenkovic, V. R.; Markovic, N. M.; Noh, T. W.; Han, S.; Mun, B. S. Role of Transition Metal in Fast Oxidation Reaction on the Pt_3TM (111) (TM = Ni, Co) Surfaces. *Adv. Energy Mater.* **2013**, *3*, 1257–1261.
13. Holewinski, A.; Idrobo, J. C.; Linic, S. High-Performance Ag-Co Alloy Catalysts for Electrochemical Oxygen Reduction. *Nat. Chem.* **2014**, *6*, 828–834.
14. Hu, G.; Nitze, F.; Gracia-Espino, E.; Ma, J.; Barzegar, H. R.; Sharifi, T.; Jia, X.; Shchukarev, A.; Lu, L.; Ma, C.; et al. Small Palladium Islands Embedded in Palladium−Tungsten Bimetallic Nanoparticles Form Catalytic Hotspots for Oxygen Reduction. *Nat. Commun.* **2014**, *5*, 5253.
15. Nørskov, J. K.; Rossmeisl, J.; Logadottir, A.; Lindqvist, L.; Kitchin, J. R.; Bligaard, T.; Jónsson, H. Origin of the Overpotential for Oxygen Reduction at a Fuel-Cell Cathode. *J. Phys. Chem. B* **2004**, *108*, 17886–17892.
16. He, Q.; Yang, X.; He, R.; Bueno-López, A.; Miller, H.; Ren, X.; Yang, W.; Koel, B. E. Electrochemical and Spectroscopic Study of Novel Cu and Fe-Based Catalysts for Oxygen Reduction in Alkaline Media. *J. Power Sources* **2012**, *213*, 169–179.
17. He, Q.; Yang, X.; Ren, X.; Koel, B. E.; Ramaswamy, N.; Mukerjee, S.; Kostecki, R. A Novel CuFe-Based Catalyst for the Oxygen Reduction Reaction in Alkaline Media. *J. Power Sources* **2011**, *196*, 7404–7410.
18. Jasinski, R. A New Fuel Cell Cathode Catalyst. *Nature* **1964**, *201*, 1212–1213.
19. Lefèvre, M.; Proietti, E.; Jaouen, F.; Dodelet, J.-P. Iron-Based Catalysts with Improved Oxygen Reduction Activity in Polymer Electrolyte Fuel Cells. *Science* **2009**, *324*, 71–74.
20. Proietti, E.; Jaouen, F.; Lefèvre, M.; Larouche, N.; Tian, J.; Herranz, J.; Dodelet, J.-P. Iron-Based Cathode Catalyst with Enhanced Power Density in Polymer Electrolyte Membrane Fuel Cells. *Nat. Commun.* **2011**, *2*, 416.
21. Li, W.; Wu, J.; Higgins, D. C.; Choi, J.-Y.; Chen, Z. Determination of Iron Active Sites in Pyrolyzed Iron-Based Catalysts for the Oxygen Reduction Reaction. *ACS Catal.* **2012**, *2*, 2761–2768.
22. Thorum, M. S.; Hankett, J. M.; Gewirth, A. A. Poisoning the Oxygen Reduction Reaction on Carbon-Supported Fe and

Cu Electrocatalysts: Evidence for Metal-Centered Activity. *J. Phys. Chem. Lett.* **2011**, *2*, 295–298.
23. *Transactions of the Metallurgical Society of AIME*; American Institute of Mining, Metallurgical, and Petroleum Engineers: New York, 1958.
24. Shafranovsky, E. A.; Petrov, Y. I.; Casas, L.; Molins, E. Structural and Mössbauer Studies of Aerosol FeCu Nanoparticles in a Wide Composition Range. *J. Nanopart. Res.* **2011**, *13*, 4913–4928.
25. Zhang, L.; Zhang, G.; Chen, C.; Li, L.; Xia, T.; Shi, K. A Facile Route To Synthesise h-BN-FeB49 Nanocomposites with Magnetic and Fluorescent Properties. *CrystEngComm* **2011**, *13*, 7153–7160.
26. Wu, G.; More, K. L.; Johnston, C. M.; Zelenay, P. High-Performance Electrocatalysts for Oxygen Reduction Derived from Polyaniline, Iron, and Cobalt. *Science* **2011**, *332*, 443–447.
27. Deng, J.; Yu, L.; Deng, D.; Chen, X.; Yang, F.; Bao, X. Highly Active Reduction of Oxygen on a FeCo Alloy Catalyst Encapsulated in Pod-like Carbon Nanotubes with Fewer Walls. *J. Mater. Chem. A* **2013**, *1*, 14868–14873.
28. Liu, H.; Wei, Y.; Sun, Y.; Wei, W. Dependence of the Mechanism of Phase Transformation of Fe(III) Hydroxide on pH. *Colloids Surf., A* **2005**, *252*, 201–205.
29. Marković, N. M.; Schmidt, T. J.; Stamenković, V.; Ross, P. N. Oxygen Reduction Reaction on Pt and Pt Bimetallic Surfaces: A Selective Review. *Fuel Cells* **2001**, *1*, 105–116.
30. Pei, P.; Ma, Z.; Wang, K.; Wang, X.; Song, M.; Xu, H. High Performance Zinc Air Fuel Cell Stack. *J. Power Sources* **2014**, *249*, 13–20.
31. Xu, Y.; Xu, X.; Li, G.; Zhang, Z.; Hu, G.; Zheng, Y. Experimental Research of Liquid Infiltration and Leakage in Zinc Air Battery. *Int. J. Electrochem. Sci.* **2013**, *8*, 11805–11813.
32. Hu, Y.; Jensen, J. O.; Zhang, W.; Cleemann, L. N.; Xing, W.; Bjerrum, N. J.; Li, Q. Hollow Spheres of Iron Carbide Nanoparticles Encased in Graphitic Layers as Oxygen Reduction Catalysts. *Angew. Chem., Int. Ed.* **2014**, *53*, 3675–9.
33. Liang, Y.; Liu, P.; Xiao, J.; Li, H.; Wang, C.; Yang, G. A Microfibre Assembly of an Iron-Carbon Composite with Giant Magnetisation. *Sci. Rep.* **2013**, *3*, 3051.
34. Lai, L.; Potts, J. R.; Zhan, D.; Wang, L.; Poh, C. K.; Tang, C.; Gong, H.; Shen, Z.; Lin, J.; Ruoff, R. S. Exploration of the Active Center Structure of Nitrogen-Doped Graphene-Based Catalysts for Oxygen Reduction Reaction. *Energy Environ. Sci.* **2012**, *5*, 7936–7942.
35. Nam, G.; Park, J.; Kim, S. T.; Shin, D. B.; Park, N.; Kim, Y.; Lee, J. S.; Cho, J. Metal-Free Ketjenblack Incorporated Nitrogen-Doped Carbon Sheets Derived from Gelatin as Oxygen Reduction Catalysts. *Nano Lett.* **2014**, *14*, 1870–1876.
36. Hohenberg, P.; Kohn, W. Inhomogeneous Electron Gas. *Phys. Rev.* **1964**, *136*, B864–B871.
37. Kohn, W.; Sham, L. J. Self-Consistent Equations Including Exchange and Correlation Effects. *Phys. Rev.* **1965**, *140*, A1133–A1138.
38. Kresse, G.; Furthmüller, J. Efficient Iterative Schemes for *Ab Initio* Total-Energy Calculations Using a Plane-Wave Basis Set. *Phys. Rev. B* **1996**, *54*, 11169–11186.
39. Kresse, G.; Furthmüller, J. Efficiency of *Ab-Initio* Total Energy Calculations for Metals and Semiconductors Using a Plane-Wave Basis Set. *Comput. Mater. Sci.* **1996**, *6*, 15–50.